Volume 17
Number 17
7 May 2021
Pages 4467–4666

Soft Matter

rsc.li/soft-matter-journal

ISSN 1744-6848

ROYAL SOCIETY OF CHEMISTRY

PAPER
Chariklia Sotiriou-Leventis, Nicholas Leventis, Hongbing Lu *et al.*
Metamaterial-like aerogels for broadband vibration mitigation

Soft Matter

PAPER

View Article Online
View Journal | View Issue

Cite this: *Soft Matter*, 2021, 17, 4496

Metamaterial-like aerogels for broadband vibration mitigation†

Sadeq Malakooti, ‡§[a] Mohammad I. Hatamleh,§[a] Rui Zhang,[a] Tahereh Taghvaee,[b] Max Miller III,[c] Yao Ren,[a] Ning Xiang,[c] Dong Qian,[a] Chariklia Sotiriou-Leventis,*[b] Nicholas Leventis¶*[b] and Hongbing Lu *[a]

Received 15th January 2021,
Accepted 23rd February 2021

DOI: 10.1039/d1sm00074h

rsc.li/soft-matter-journal

We report a mechanical metamaterial-like behavior as a function of the micro/nanostructure of otherwise chemically identical aliphatic polyurea aerogels. Transmissibility varies dramatically with frequency in these aerogels. Broadband vibration mitigation is provided at low frequencies (500–1000 Hz) through self-assembly of locally resonant metastructures wherein polyurea microspheres are embedded in a polyurea web-like network. A micromechanical constitutive model based on a discrete element method is established to explain the vibration mitigation mechanism. Simulations confirm the metamaterial-like behavior with a negative dynamic material stiffness for the micro-metastructured aerogels in a much wider frequency range than the majority of previously reported locally resonant metamaterials.

1. Introduction

Metamaterials show unusual physical properties deriving from their structure rather than their chemical composition.[1,2] Such properties include negative Poisson's ratios,[3] negative thermal expansion coefficients,[4] and negative refractive indexes.[5] Applications span from ultra-stiff structural materials[6–8] to programmable soft robots.[9–11] One particular class of metamaterials of interest for vibration control and sound insulation applications[12–17] shows low-frequency bandgaps induced by local resonators.[2,18–22] However, in practice, those bandgaps are either at discrete frequencies, or they appear only over narrow frequency ranges, and usually only in a specific direction of sound/vibration propagation.[21,23–26] Meanwhile, "broadband" wave attenuation with metamaterials is of interest for various engineering applications including vibration mitigation.[19,27] Such broadband wave attenuation has been achieved and is reported here with certain aliphatic polyurea (PUA) aerogels. The metamaterial-like behavior of these aerogels is derived from their innate locally resonant micro/nanostructures.

While silica aerogels, the most well-known class of these materials, have not been established beyond thermal insulation,[28–30] low-cost highly ductile polymeric aerogels warrant further consideration.[31] Commercially available aliphatic polyurea aerogels,[32,33] for example, have been investigated for explosive shockwave mitigation.[34,35] In the same context, polyurea aerogels chemically identical to the commercial samples, but with an intriguing cocoon-in-web morphology,[36] have been investigated for acoustic attenuation;[37–39] Lu *et al.*, for example, have reported sound transmission loss values of over 30 dB cm^{-1} over the range of 1 to 4 kHz for 5 mm thick polyurea aerogel samples with that morphology, but most importantly it was noted that the microstructure of those materials had striking similarities with acoustic metamaterials.[38] Based on these results, the same authors introduced polyurea aerogels of different bulk densities and porosities into laminated composites in the form of thin sheets, for example between two gypsum wallboards of the type typically used in soundproofing applications,[39] and reported that the random-incidence sound transmission loss (STL) of the sandwich structure reached 40 dB cm^{-1} at 2 kHz; most interestingly, however, that performance was achieved without a significant increase of the panel mass or the wall thickness, just by stacking only two 5 mm-thick aerogel layers of bulk densities of 0.15 and 0.25 g cm^{-3}, respectively.[39]

Recently, Leventis *et al.* reported that polyurea aerogels with the same chemical composition as the materials used in all the studies summarized in the previous paragraph can actually be prepared with a very wide range of nano- and micro-morphologies, which could be characterized by a *unique*

[a] *Department of Mechanical Engineering, The University of Texas at Dallas, Richardson, TX 75080, USA. E-mail: hongbing.lu@utdallas.edu*
[b] *Department of Chemistry, Missouri University of Science and Technology, Rolla, MO 65409, USA. E-mail: cslevent@mst.edu, nleventis@aerogel.com*
[c] *Graduate Program in Architectural Acoustics, Rensselaer Polytechnic Institute, Troy, NY 12180, USA*

† Electronic supplementary information (ESI) available. See DOI: 10.1039/d1sm00074h

‡ Current address: NASA Glenn Research Center, 21000 Brookpark Rd, Cleveland, OH 44135, USA.
§ These authors contributed equally to this work.
¶ Current address: Aspen Aerogels, Inc., 30 Forbes Road, Bldg B, Northborough, MA 01532, USA.

numerical identifier, referred to as the *K*-index. The *K*-index quantifies the nanostructure *via* its porosity (Π, as a proxy for the openness) and the water contact angle (θ, as a proxy for texture) and is defined as the θ/Π ratio. The *K*-index can be readily measured and the use of the *K*-index has provided a novel methodology for the synthesis of polyurea aerogels with any microstructure at will.[40] Therefore, with deterministic procedures available for the preparation of a wide variety of polyurea nanostructures, here we set out to investigate the vibration insulation performance of polyurea aerogels as a function of nanostructures.

From an acoustics point of view, the compressive waves might seem irrelevant as typically the bending waves are more important than compressive waves for blocking sound wave propagations in a wall panel in a building or vehicle. Standardized testing sound transmission loss of a wall panel requires a sample panel, typically 10 m^2 in size, as specified in ASTM standard E90-90,[41] which is similar to ISO 10140.[42] Testing for each formulation using a 10 m^2 wall panel incorporating an aerogel layer in a sandwich panel is a major task, and very costly. To date, to the best of our knowledge, the only E90 testing on a wall panel incorporating aerogels reported in open literature was the one we reported.[39] A gypsum board with the use of a polyurea aerogel has increased the sound transmission loss higher than 6 dB over the control gypsum board without the use of the polyurea aerogel, indicating a significant broadband sound attenuation under a predominantly bending wave in a wall panel. A viable acoustic transmission loss material for use in a wall panel has to first pass the sound transmission loss test for compressive waves. In addition, in many other applications such as earphones and earmuffs, the compressive waves are still dominant. With these considerations, this work will focus on the characterization of the compressive wave propagation in the polyurea aerogels.

Accordingly, we considered the vibration insulation performance of four distinctly different nanomorphologies of the same aliphatic triisocyanate-derived polyurea. These four aerogels are: caterpillar-like assemblies of nanoparticles (*K*-index = 1.2), random assemblies of nanoparticles (*K*-index = 1.4), entangled nanofibers (*K*-index = 1.6), and microspheres embedded in hair-like fibers (*K*-index = 1.8).[40] The latter two nanostructures were selected specifically in order to bracket the cocoon-in-web nanostructure of polyurea (*K*-index = 1.7) with which it was noted that the STL of polyurea aerogels was similar to that of acoustic metamaterials.[38] ''Bracketing'' refers to increasing the ''web'' component of the cocoon-in-web structures by moving to an exclusively fibrous structure with *K*-index = 1.6, or the ''cocoon'' component by increasing the size of the spheres embedded in fibers (*K*-index = 1.8).

2. Results and discussion

2.1. Aerogel preparation and general material properties

Polyurea (PUA) aerogels were prepared *via* reaction of a commercially available aliphatic triisocyanate (Desmodur N3300A) and water using triethylamine as catalyst, as described previously.[40] The nanomorphology was varied in a pre-determined fashion by varying the monomer and catalyst concentration, but primarily the solvent. Caterpillar-like assemblies of nanoparticles (*K*-index = 1.2, Fig. 1A) and random assemblies of nanoparticles (*K*-index = 1.4, Fig. 1B) were obtained in acetone, while entangled nanofibers (*K*-index = 1.6, Fig. 1C), and microspheres embedded in hair-like fibers (*K*-index = 1.8, Fig. 1D) were obtained in acetonitrile. The SEM micrographs of the samples are shown in Fig. 1.

The general material properties of PUA aerogels including bulk density, porosity, BET surface area, and Young's modulus of the four different morphologies in Fig. 1 are summarized in Table 1. A more extensive list of properties including the specific energy absorption and thermal conductivity is presented in Tables S1–S3 of the ESI.† Attention was paid to the sample selection so that the bulk densities would match one another closely. That was not possible with the entangled nanofiber morphology (*K*-index = 1.6), which is observed only with lower monomer concentration formulations.[40] Nevertheless, porosities (as a percent of empty space) were reasonably close. Specific surface areas of nanoparticulate samples (with *K*-indexes equal to 1.2 and 1.4) were multiple times higher than those of the fibrous samples (with *K*-indexes equal to 1.2 and 1.4), reflecting that very morphological difference. Finally, reflecting the relative interconnectivity of nanoparticles *versus* nanofibers, the Young's moduli of the nanoparticulate samples were multiple times higher than those of the samples that include fibers.

2.2. Vibration transmissibility

Using an electromagnetic shaker, PUA aerogel samples at nominal dimensions of 50 × 50 × 5 mm with the morphologies shown in Fig. 1 were excited with a log-sweep signal from 0.1 to 1000 Hz and accelerations at the two ends of the samples were measured. For a one-dimensional experimental vibration

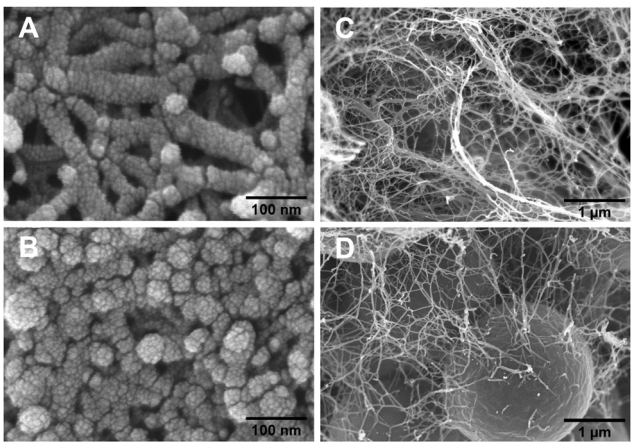

Fig. 1 Four distinct morphology groups for aliphatic polyurea aerogels with identical chemical composition: (A) caterpillar-like assemblies of nanoparticles (*K*-index = 1.2); (B) random assemblies of nanoparticles (*K*-index = 1.4); (C) entangled nanofibers (*K*-index = 1.6); (D) microspheres-with-''hair'' (*K*-index = 1.8). For other relevant material properties see Table 1.

Table 1 General material properties of the polyurea aerogels

Morphology	Bulk density[a] (ρ_b, g cm^{-3})	Porosity[b] (Π, % v/v)	BET surf. area (σ, m^2 g^{-1})	Young's modulus (E, MPa)
Caterpillar-like assemblies of nanoparticles	0.150 ± 0.002	87.5 ± 0.5	185	36 ± 1
Random assemblies of nanoparticles	0.277 ± 0.002	76.9 ± 0.2	151	82 ± 3
Entangled nanofibers	0.062 ± 0.001	94.8 ± 1.7	60	2.1 ± 0.1
Microspheres-with-"hair"	0.151 ± 0.009	87.2 ± 0.8	23	6.3 ± 0.4

[a] Average of 3 samples. [b] Porosity (percent of empty space) $\Pi = 100 \times (\rho_s - \rho_b)/\rho_s$, where ρ_s is the skeletal density of the PUA aerogels measured with He pycnometry and found in the range of 1.18–1.20 g cm^{-3} for all samples.

analysis through the thickness, a thin sample geometry was considered. The experimental setup is shown in Fig. S1 of the ESI.† The transmissibility (T) is defined as the complex ratio of the top acceleration (a_T) over the bottom acceleration (a_B) signals. Fig. 2 shows the transmissibility in dB, $T = 10\log(|a_T/a_B|)$, for all four morphologies of PUA aerogels selected for this study, as a function of frequency. The difference between the vibration transmissibility of these samples is immediately noticeable. The transmissibility of PUA aerogels consisting of caterpillar-like assemblies of nanoparticles (K-index = 1.2) and random assemblies of nanoparticles (K-index = 1.4) show a resonance and an anti-resonance feature at the low-frequency band (about 200 Hz). Although the isolation characteristics (*i.e.*, negative transmissibility) of these samples are limited, their broad amplification characteristics (*i.e.*, positive transmissibility) at the high-frequency range (500 to 1000 Hz) are intriguing for engineering applications such as in speakers and energy harvesters. For this purpose, a thorough vibration amplification analysis of these samples at different configurations including their composite lay-ups (*e.g.*, panels with caterpillar-like and random assemblies of nanoparticles) would be required, which is outside the scope of this work.

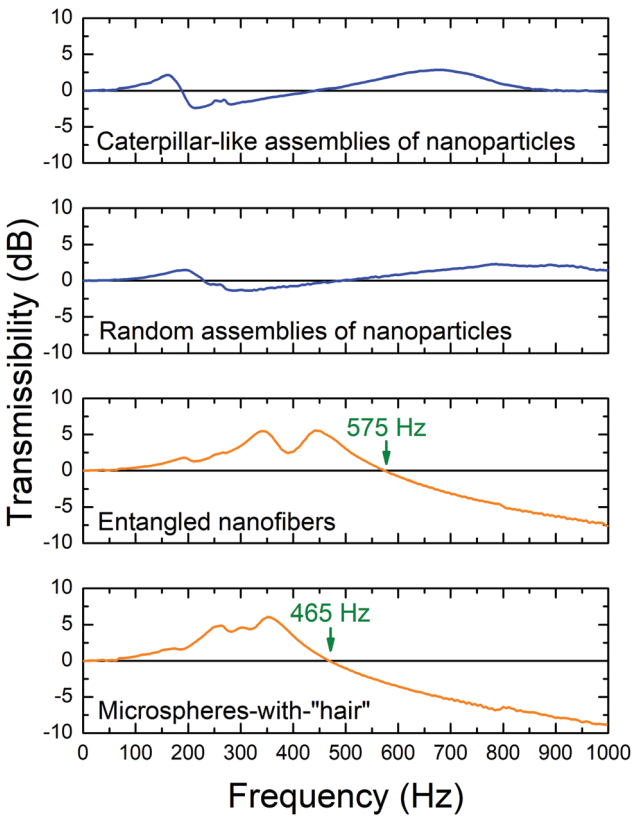

Fig. 2 Vibration transmissibility for chemically identical polyurea aerogel samples (each 5 mm thick) at different morphologies as described within the frames (refer also to Fig. 1).

On the other hand, PUA aerogels consisting of entangled nanofibers and microspheres-with-"hair" show a resonance feature followed by a broadband vibration mitigation for almost half of the excitation frequency range. PUA aerogels consisting of microspheres-with-"hair" (K-index = 1.8) exhibit the widest mitigation frequency band among other morphologies. However, we cannot but also notice the complementarity of the transmissibility spectra as a function of nanomorphology. It is worth mentioning again that the chemical composition and sample size of all samples are either the same or close. However, the broadband vibration mitigation response of the PUA aerogel with microspheres-with-"hair" (K-index = 1.8) morphology cannot be explained in terms of sample's bulk density and/or modulus. As one can see from Table 1, the sample with microspheres-with-"hair" (K-index = 1.8) morphology has a similar bulk density to the sample with caterpillar-like assemblies of nanoparticles (K-index = 1.2) but their vibration responses are completely different. In addition, the Young's modulus of the sample with microspheres-with-"hair" (K-index = 1.8) morphology is three times higher than the modulus of the sample with entangled fibers (K-index = 1.6) morphology but shows a wider mitigation frequency band. This means that the overall similarity in the transmissibility of the samples with entangled nanofibers and microspheres-with-"hair" morphologies should not be translated to a dominant role for fibers. Therefore, we conclude that the difference in vibration insulation properties of those aerogels should be a morphology driven phenomenon that needs to be elaborated by material modeling at the microstructural level.

2.3. Micromechanical constitutive modeling

Although both fibrous and microspheres-with-"hair" structures provide broadband mitigation, it is reasonable to assume that the microspheres in the latter structure would act as an embedded resonator, and therefore the mitigation frequency range would become broader compared to the sample consisting of entangled nanofibers. Based on this reasoning, the PUA aerogels with microsphere-with-"hair" morphologies were modeled using the Discrete Element Method (DEM).[43–45] Accordingly, the PUA

microspheres with diameters consistent with the SEM micrographs were randomly packed at similar bulk density and porosity as in the corresponding PUA aerogel sample. The contact interactions between the particles which primarily come from the effect of fibers in microsphere-with-"hair" morphologies were modeled using linear contact stiffness. Indeed, there might be a small deviation between the model and the actual structure, nevertheless the model captures the essential feature of the actual structure, namely that it consists of spheres connected with fibers (simulated by springs), and in that respect it was considered adequate. No intrinsic damping was included in this model. All DEM-based simulations were carried out using the commercial package Abaqus/Standard 6.14 (Dassault Systems). The strategies for the creation and initialization of the DEM models are shown in Fig. S2 of the ESI.† A model with approximately 10 000 microspheres was considered. The long-range interactions of the model with more than 5000 microspheres are converged (see Fig. S3, ESI†). The optimum particle contact stiffness (10 N m^{-1}) was obtained using the 10k model by comparing the computational Young's modulus results against the experimental Young's modulus value. The percent error between the experimental and computational Young's moduli was approximately 1.5%. Next, using a similar approach, with the fixed contact stiffness of 10 N m^{-1}, we studied the effect of computational domain size in terms of the number of particles and the effective Young's modulus of the aerogel. The aspect ratio of the computational box was chosen to be the same as the aspect ratio of the actual samples. It was found that a minimum of 5k particles (which is equivalent to a computational domain size of 40 × 80 × 80 μm) is required to provide converging results for the effective Young's modulus from the proposed micromechanical model (see Fig. S3 in the ESI†). At the end, dynamic simulations were carried out with a model containing 5150 particles. Under dynamic conditions, as the experimental transmissibility signal shows, there is a resonance feature before the isolation frequency. The contact stiffness value obtained from the quasi-static simulations showed a resonance feature at frequencies much lower than the actual resonance frequency of the material. Therefore, in order to capture the dynamic behavior of the PUA material with microsphere-with-"hair" morphology, the static model parameters had to be tuned. Based on the experimental transmissibility of the PUA aerogels with the microspheres-with-"hair" morphology (see Fig. 2), the resonance characteristic feature starts from 200 to 450 Hz. This is a broad linewidth that points at the existence of multiple underlying or internal resonance frequencies. Therefore, the model was updated with multiple contact stiffness values for particle–particle interactions. Through some iterative simulations with a model formed by different stiffness values, it was found that the major resonance feature can be reconstructed effectively with only two stiffness values of 800 and 2000 N m^{-1}. Compared to quasi-static contact stiffness, the higher values for dynamic stiffness are in agreement with dynamic hardening mechanisms in time-dependent materials, *e.g.* ref. 46. The stiffness values were then assigned randomly to the particle–particle contact springs of the model at different percentages. In our micromechanical model, there are about 38k massless springs. Through an optimization

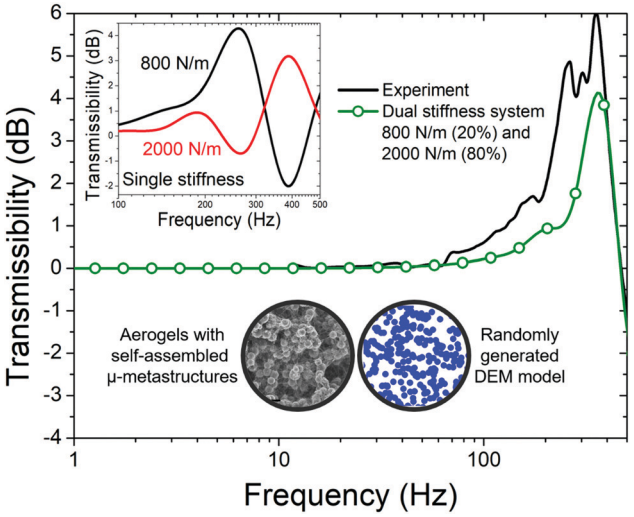

Fig. 3 Comparison of experimental vibration transmissibility (dB) of a PUA aerogel sample with a microspheres-with-"hair" morphology (refer to Fig. 1), with the micromechanical model prediction at the low-frequency range. The micromechanical DEM based model contains 5150 randomly packed spherical PUA particles with approximately 38k massless contact springs with 800 N m^{-1} (20% of the springs) and 2000 N m^{-1} (80% of the springs) stiffness values. Inset: Transmissibility of the same model with the two discrete stiffness values of 800 N m^{-1} and 2000 N m^{-1}.

procedure, it turned out that the micromechanical model with 20% of springs with stiffness values of 800 N m^{-1} and the rest (80%) with 2000 N m^{-1}, provides an agreement with resonance and isolation features compared with the experimental transmissibility signal. Fig. 3 shows the experimental transmissibility signal and the micromechanical model reconstructed transmissibility of the PUA aerogel with the microsphere-with-"hair" morphology. A view from an SEM micrograph of the sample with the microsphere-with-"hair" morphology at a lower magnification and an image from the randomly generated DEM model are displayed as an inset in Fig. 3. The full SEM micrograph of the sample with the microsphere-with-"hair" morphology at the lower magnification is shown in Fig. S4 of the ESI.† Moreover, the transmissibility response of the micromechanical model with uniform stiffness values of 800 and 2000 N m^{-1} are also shown as an inset in Fig. 3.

2.4. Vibration mitigation mechanism

Traditionally, in experimental modal analysis of a multi-degree-of-freedom system, classical types of damping mechanisms such as structural, viscous, and Coulomb damping forms were represented by a hypothetical form of damping component proportional to the system mass and stiffness. However, using our microstructurally, as well as experimentally driven model, we are able to study the nature of the material's damping response to the external stimuli at a microstructural level. Here, as we did not include any type of "material" damping in the modeling, the vibration isolation mechanism must be a structurally related phenomenon. This is indeed in agreement with our experimental observations where all tested materials are chemically similar but at different microstructures. For this purpose, we first study the coupling force fields at several

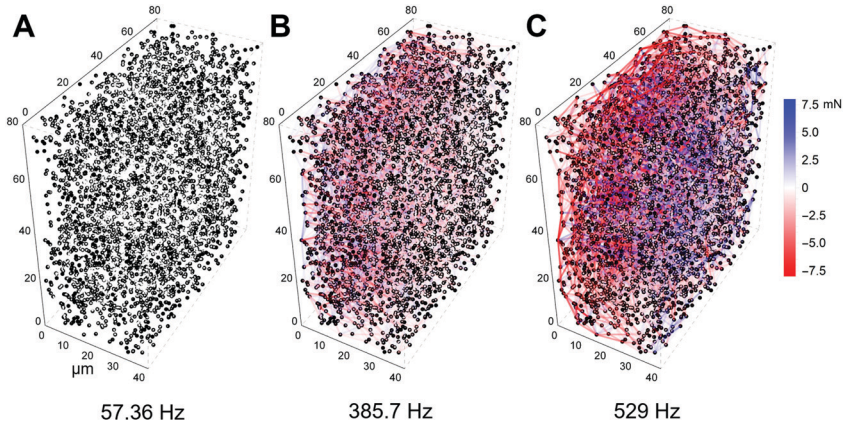

Fig. 4 The particle coupling force fields in the PUA aerogel micromechanical model at three frequencies corresponding to: (A) low-frequency, (B) resonance, and (C) isolation zones. Tensile and compressive forces are shown by blue and red colors, respectively. Force fields are shown in their undeformed configurations.

excitation frequencies. Fig. 4 shows the coupling forces between the aerogel particles at three frequencies of 57.36 Hz, 385.7 Hz, and 529 Hz which are corresponding to low-frequency, resonance, and isolation zones, respectively. The force magnitude (tensile forces are positive while compressive forces are negative) is increasing with the increase in excitation frequency. At the low-frequency zone (Fig. 4A) where the system is close to its rigid body motion state, the material does not feel any internal load. Therefore, it does not have any deformation and no dissipation happened towards vibration transmission. However, at higher frequencies, the material starts to react to the incoming mechanical vibrations. It is interesting that the maximum force magnitude at 529 Hz (isolation zone) is almost three times higher than the one at 385.7 Hz (resonance zone). This agrees with the fact that at isolation frequency (Fig. 4C), the material must dampen the entire incoming mechanical vibration which leads to a higher force magnitude at the isolation frequency than the resonance frequency of the material.

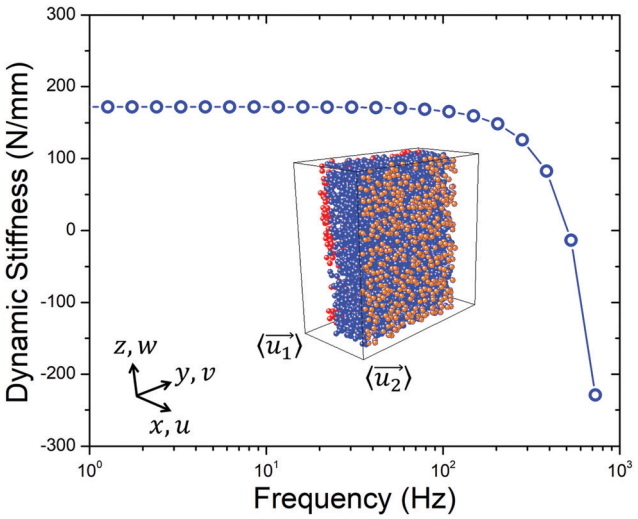

Fig. 5 Dynamic stiffness of the PUA aerogel material model as a function of the excitation frequency. The micromechanical model proposes the existence of negative global dynamic stiffness for the monolithic aerogels with microspheres-with-"hair" morphology at the vicinity of isolation frequency. The coordinates along with a 3D view of the micromechanical model are also shown in the inset.

In order to translate the dynamic micro-force fields shown in Fig. 4 to the global dynamic behavior of the aerogels, their dynamic mass and dynamic stiffness as a function of frequency were calculated and studied. The dynamic mass of the aerogel model was found to be the same as the static mass of the model (results are not shown here). In order to calculate the global dynamic stiffness as a function of frequency, k_d, the total force along the x-axis, F_x, and the net deformation along the x-axis, δu, were calculated at each excitation frequency. F_x is calculated by the sum of the force components along the x-axis for the material model particles located at the loading edge-group zone (these particles are shown with red color in the inset of Fig. 5). Also, δu is the difference between the average displacements along the x-axis of both edge-group particles, $|\overrightarrow{u_2} - \overrightarrow{u_1}|$, shown with red and orange colors in the inset of Fig. 5. Finally, the global dynamic stiffness then becomes $k_d = F_x/\delta u$. Fig. 5 shows the dynamic stiffness of the aerogel material model as a function of the excitation frequency. Fascinatingly, the micromechanical model reveals the presence of a negative global dynamic stiffness as the aerogel's vibration mitigation mechanism. Previously, a negative dynamic stiffness is only reported in metamaterials with a specifically designed structure.[1,2,22] This is the first sign of the presence of broadband negative dynamic stiffness in a self-assembled monolithic material. A sudden though continuous decrease in the dynamic stiffness is striking. The decrease in dynamic stiffness starts from the resonance frequencies and drastically drops at the vicinity of isolation frequency. This study shows the feasibility in providing a metamaterial-like behavior from a monolithic material with systematic microstructural tailoring.

3. Conclusions

The investigation of the microstructural effects on the dynamic macroscopic behavior of materials, especially at low

frequencies, is not a straightforward task, and comparison between materials is difficult. Herein, we have eliminated the uncertainty associated with chemical composition by measuring the vibration transmissibility of polyurea (PUA) aerogels with identical chemical composition but different micromorphology. PUA aerogels with entangled nanofibers and microspheres-with-"hair" morphologies showed broadband vibration mitigation, while samples with caterpillar-like and random assemblies of nanoparticles did not show any significant vibration isolation. This observation resonates with the presence of an underlying microstructure-driven vibration mitigation mechanism. Using a micromechanical model, PUA aerogels consisting of microspheres-with-"hair" were modeled and studied. With no material pre-damping consideration, the model suggested a metamaterial-like behavior in terms of a broadband negative dynamic stiffness solely originating from the innate metastructure of these aerogels. This work may pave the way towards manufacturing more effective metamaterials by tailoring their microstructures for applications in acoustic transmission loss in earplugs and earphones, and perhaps acoustic panels on a significantly larger scale.

4. Experimental section

Transmissibility measurements

In this experiment, the aerogel sample at nominal dimensions of $50 \times 50 \times 5$ mm^3 is sandwiched and is excited through the bottom plate by a permanent magnet electrodynamic shaker (B&K V455). The measurement configuration is shown in Fig. S1 of the ESI.† The input signal is a log sweep to excite a broadband spectrum from 0.1 to 1000 Hz. The transmissibility T is defined as the complex ratio of the accelerations at the top and bottom plates. The applied load (F) and acceleration of the shaker (a_B) are simultaneously measured by an impedance sensor (PCB Piezotronics, ICP® impedance head 288D01) and the top load mass acceleration (a_T) is measured simultaneously by another accelerometer (PCB Piezotronics, Model 352C33). The DAQ assistance VI in the LabVIEW program is used to generate signals and record the accelerations. A log-sweep-sine signal is output from LabVIEW software through a data acquisition board (DAQ, NI BNC2110), which is sent to an amplifier (LDS LPA 100). The amplified signal is then sent to the shaker. A signal conditioner (PCB Piezotronics, Model 482C15) is used to increase the amplitude of the accelerometer and impedance head signals, which are sent back to the DAQ and collected by LabView software. A sampling frequency of 20 kHz was used in the tests, well above the necessary Nyquist frequency so that potential higher-order harmonics in the system could be detected. The number of points (FFT size) in the data was set to 16 384, and ten averages were taken for each round of data collection. The transmissibility T is then determined in dB as $T = 10\log(|a_T/a_B|)$.

Basic material characterization

Bulk densities (ρ_b) were determined from the weight and the physical dimensions of the samples. Skeletal densities (ρ_s) were determined with helium pycnometry using a Micromeritics AccuPyc II 1340 instrument. Samples for skeletal density measurements were outgassed for 24 h at room temperature under vacuum before analysis. Porosities (Π) as a percent of empty space were determined from the ρ_b and p_s values *via* $\Pi = 100 \times [(p_s - \rho_b)/p_s]$. Quasi-static compression tests were performed on an Instron mechanical testing system (Instron Inc., Model 5969, Norwood, MA) with 500 N load cell (with accuracy of 0.5% of the reading). The compression rate was set to 0.5 mm min^{-1}. Cylindrical-shaped samples with 20 mm diameter and 20 mm height were drilled out from a larger PU aerogel sample.

SEM microscopy

SEM images were captured from Au/Pd (60/40) coated samples on a Hitachi Model S-4700 field emission microscope.

5. Simulations

Construction of the micromechanical model

For this purpose, a MATLAB code (generateGeom) was written to generate a given number of spherical particles which are randomly packed inside a computational box at given box dimensions. The initial geometrical parameters such as average particle diameter and average particle distance were estimated using the corresponding SEM image (Fig. 1D). The average diameter and distance of the spherical particles were measured to be 2.3 ± 0.2 μm and 2.3 ± 0.7 μm, respectively. The average particle mass was calculated using the previously reported skeletal density for the polyurea aerogels (1.2 g cm^{-3}) and their average diameter. The computational domain size is then calculated using a given number of particles and the average particle mass at a similar aspect ratio to the experimental sample (1 : 1 : 1/2). Next, all randomly packed particles are connected by a linear contact spring to their neighbors with a distance less than a cutoff length (check Fig. S2-B of the ESI†). Conceptually, this length is related to the degree of fiber entanglement, which was estimated from the average length of the fibers in the samples consisting of microspheres-with-"hair" (refer to Fig. S4 in the ESI†). The cutoff length was assumed to be 12 μm. Finally, using a Python script (springMassSystem), the material model was imported into Abaqus/Standard 6.14 for DEM analysis.

Quasi-static simulations

The compressive behavior was simulated using the commercial package Abaqus/Standard 6.14 (Dassault Systems). For this purpose, a finite-sized computational model at similar bulk density and porosity of the experimental sample was constructed. The particles were grouped into three zones (two edge-groups shown in orange and red, and one core-group shown in blue) as shown with different colors in Fig. S2-C in the ESI.† The edge-group particles were used to apply the boundary and loading conditions. Under a displacement control simulation, the red edge-group particles were fixed (encastré boundary condition) and the orange

edge-group particles were subjected to a compressive displacement along the model thickness. The effective stress–strain curve of the model up to −20% compressive strain was determined in order to obtain the effective Young's modulus. The effective Young's moduli of micro-computational models at different number of particles but at the same bulk density and porosity were calculated and shown in Fig. S3 of the ESI.† For this purpose, the average spring stiffness of the particle–particle DEM interactions was determined to be 10 N m^{-1} (check Fig. S2-A of the ESI†). As the size of the micro-computational models grows (here the size is expressed in terms of the number of particles in the model), the mechanical behavior of the micro-computational models is isotopically homogenized and the effective Young's moduli are converging to the average experimental Young's modulus for the aerogel sample (6.5 MPa). As the computational cost is proportional to the number of particles, using Fig. S3 of the ESI,† we determined the minimum number of particles (∼5k particles) with accurate results. Therefore, for dynamic simulations, the micromechanical models with 5150 particles were used to determine the dynamic material properties of micro-metastructures.

Dynamic simulations

For this purpose, the computational model with 5150 particles at similar bulk density and porosity of the experimental sample was used. The particles were grouped into three zones similar to the quasi-static simulations. The edge-group particles were used to apply the boundary and loading conditions. A free boundary condition was set for both ends. Under a displacement control simulation, the red edge-group particles were subjected to a log-swept sinusoidal displacement with a frequency ranging from 0.1 to 1000 Hz along the model thickness direction and the displacement response at the other edge was calculated. The transmissibility was then calculated in dB from the ratio of the average accelerations of each edge particle groups.

Code availability

The code used for DEM model initiation and analysis has been archived in a GitHub repository (https://github.com/sadeqmalakooti/AerogelMicromechanics.git).

Conflicts of interest

The authors declare no conflict of interest.

Acknowledgements

We thank the NSF under award numbers CMMI-1661246, CMMI-1636306, CMMI-1726435, CMMI-1727960 and CMMI-1530603 (sub-contract to MS&T from Tufts University), Sandia National Laboratories grant (220202), the Army Research Office (W911NF-14-1-0369) for financial support, and Covestro LLC (formerly Bayer Corporation USA) for the generous supply of Desmodur N3300A. R. Zhang is grateful for the support from the Eugene McDermott Graduate Fellowship from The University of Texas at Dallas. H. Lu is also grateful for the support from the Louis Beecherl Jr. Endowed Chair.

References

1 Y. Liu and X. Zhang, *Chem. Soc. Rev.*, 2011, **40**, 2494–2507.
2 G. Ma and P. Sheng, *Sci. Adv.*, 2016, **2**, e1501595.
3 J.-H. Lee, J. P. Singer and E. L. Thomas, *Adv. Mater.*, 2012, **24**, 4782–4810.
4 Q. Wang, J. A. Jackson, Q. Ge, J. B. Hopkins, C. M. Spadaccini and N. X. Fang, *Phys. Rev. Lett.*, 2016, **117**, 175901.
5 N. Kaina, F. Lemoult, M. Fink and G. Lerosey, *Nature*, 2015, **525**, 77–81.
6 X. Zheng, H. Lee, T. H. Weisgraber, M. Shusteff, J. DeOtte, E. B. Duoss, J. D. Kuntz, M. M. Biener, Q. Ge, J. A. Jackson, S. O. Kucheyev, N. X. Fang and C. M. Spadaccini, *Science*, 2014, **344**, 1373–1377.
7 K. Bertoldi, V. Vitelli, J. Christensen and M. Van Hecke, *Nat. Rev. Mater.*, 2017, **2**, 1–11.
8 W. Zhang, J. Chen, X. Li and Y. Lu, *Small*, 2020, **16**, 2004190.
9 J. L. Silverberg, A. A. Evans, L. McLeod, R. C. Hayward, T. Hull, C. D. Santangelo and I. Cohen, *Science*, 2014, **345**, 647–650.
10 C. Coulais, E. Teomy, K. De Reus, Y. Shokef and M. Van Hecke, *Nature*, 2016, **535**, 529–532.
11 B. Florijn, C. Coulais and M. Van Hecke, *Phys. Rev. Lett.*, 2014, **113**, 175503.
12 K. H. Matlack, A. Bauhofer, S. Krödel, A. Palermo and C. Daraio, *Proc. Natl. Acad. Sci. U. S. A.*, 2016, **113**, 8386–8390.
13 B. Assouar, M. Oudich and X. Zhou, *C. R. Phys.*, 2016, **17**, 524–532.
14 G. Gantzounis, M. Serra-Garcia, K. Homma, J. M. Mendoza and C. Daraio, *J. Appl. Phys.*, 2013, **114**, 093514.
15 Y. Chen and L. Wang, *Sci. Rep.*, 2015, **5**, 1–11.
16 T. Brunet, A. Merlin, B. Mascaro, K. Zimny, J. Leng, O. Poncelet, C. Aristégui and O. Mondain-Monval, *Nat. Mater.*, 2015, **14**, 384–388.
17 T. Brunet, K. Zimny, B. Mascaro, O. Sandre, O. Poncelet, C. Aristégui and O. Mondain-Monval, *Phys. Rev. Lett.*, 2013, **111**, 264301.
18 N. Kaina, A. Causier, Y. Bourlier, M. Fink, T. Berthelot and G. Lerosey, *Sci. Rep.*, 2017, **7**, 1–11.
19 P. Wang, F. Casadei, S. Shan, J. C. Weaver and K. Bertoldi, *Phys. Rev. Lett.*, 2014, **113**, 014301.
20 B. L. Davis and M. I. Hussein, *Phys. Rev. Lett.*, 2014, **112**, 055505.
21 Z. Liu, X. Zhang, Y. Mao, Y. Y. Zhu, Z. Yang, C. T. Chan and P. Sheng, *Science*, 2000, **289**, 1734–1736.
22 X. Zhou, X. Liu and G. Hu, *Theor. Appl. Mech. Lett.*, 2012, **2**, 041001.
23 S. A. Cummer, J. Christensen and A. Alù, *Nat. Rev. Mater.*, 2016, **1**, 1–13.
24 N. Fang, D. Xi, J. Xu, M. Ambati, W. Srituravanich, C. Sun and X. Zhang, *Nat. Mater.*, 2006, **5**, 452–456.

25 C. Lagarrigue, J. P. Groby, V. Tournat, O. Dazel and O. Umnova, *J. Acoust. Soc. Am.*, 2013, **134**, 4670–4680.
26 H. Kim, Y. Cang, E. Kang, B. Graczykowski, M. Secchi, M. Montagna, R. D. Priestley, E. M. Furst and G. Fytas, *Nat. Commun.*, 2018, **9**, 1–11.
27 Y. Chen, T. Li, F. Scarpa and L. Wang, *Phys. Rev. Appl.*, 2017, **7**, 024012.
28 M. M. Koebel, A. Rigacci and P. Achard, *Aerogels Handbook*, Springer, New York, 2011, pp. 607–633.
29 E. Moretti, F. Merli, E. Cuce and C. Buratti, *Energy Procedia*, Elsevier Ltd, 2017, vol. 111, pp. 472–480.
30 F. Sabri, M. E. Sebelik, R. Meacham, J. D. Boughter, M. J. Challis and N. Leventis, *PLoS One*, 2013, **8**, e66348.
31 M. A. Aegerter, N. Leventis and M. M. Koebel, *Aerogels Handbook*, Springer New York, New York, NY, 2011, pp. 891–892.
32 N. Leventis, C. Sotiriou-Leventis, N. Chandrasekaran, S. Mulik, Z. J. Larimore, H. Lu, G. Churu and J. T. Mang, *Chem. Mater.*, 2010, **22**, 6692–6710.
33 N. Leventis, C. Sotiriou-Leventis and S. Mulik, *Three-dimensional porous polyurea networks and methods of manufacture*, US10301445B2, 2011.
34 M. A. Price, T. D. Aslam and J. J. Quirk, *AIP Conference Proceedings*, American Institute of Physics Inc., 2018, vol. 1979, p. 110016.
35 N. Whitworth and B. Lambourn, *AIP Conference Proceedings*, American Institute of Physics Inc., 2018, vol. 1979, p. 030007.
36 N. Leventis, C. Chidambareswarapattar, A. Bang and C. Sotiriou-Leventis, *ACS Appl. Mater. Interfaces*, 2014, **6**, 6872–6882.
37 United States Patent, US9068346B1, 2013, US Patent # 9,068,346 B1.
38 S. Malakooti, H. G. Churu, A. Lee, T. Xu, H. Luo, N. Xiang, C. Sotiriou-Leventis, N. Leventis and H. Lu, *J. Non-Cryst. Solids*, 2017, **476**, 36–45.
39 S. Malakooti, H. G. Churu, A. Lee, S. Rostami, S. J. May, S. Ghidei, F. Wang, Q. Lu, H. Luo, N. Xiang, C. Sotiriou-Leventis, N. Leventis and H. Lu, *Adv. Eng. Mater.*, 2018, **20**, 1700937.
40 T. Taghvaee, S. Donthula, P. M. Rewatkar, H. Majedi Far, C. Sotiriou-Leventis and N. Leventis, *ACS Nano*, 2019, **13**, 3677–3690.
41 ASTM E90 - Standard Test Method for Laboratory Measurement of Airborne Sound Transmission Loss of Building Partitions and Elements, 2016.
42 ISO 10140-1 - Acoustics—Laboratory measurement of sound insulation of building elements, 2010.
43 H. P. Zhu, Z. Y. Zhou, R. Y. Yang and A. B. Yu, *Chem. Eng. Sci.*, 2007, **62**, 3378–3396.
44 H. P. Zhu, Z. Y. Zhou, R. Y. Yang and A. B. Yu, *Chem. Eng. Sci.*, 2008, **63**, 5728–5770.
45 P. M. Pieczywek and A. Zdunek, *Soft Matter*, 2017, **13**, 7318–7331.
46 J. Zhang, N. Kikuchi, V. Li, A. Yee and G. Nusholtz, *Int. J. Impact Eng.*, 1998, **21**, 369–386.